In Situ Scanning Transmission Electron Microscopy Observations of Fracture at the Atomic Scale

Lingli Huang [1,*], Fangyuan Zheng,[2,*] Qingming Deng [3,*], Quoc Huy Thi [1,*], Lok Wing Wong [2], Yuan Cai,[4]
Ning Wang,[4] Chun-Sing Lee,[1] Shu Ping Lau,[2] Manish Chhowalla,[5] Ju Li,[6] Thuc Hue Ly [1,7,†] and Jiong Zhao [2,8,‡]

[1]*Department of Chemistry and Center of Super-Diamond & Advanced Films (COSDAF), City University of Hong Kong, Kowloon, Hong Kong, China*
[2]*Department of Applied Physics, The Hong Kong Polytechnic University, Kowloon, Hong Kong, China*
[3]*Physics department and Jiangsu Key Laboratory for Chemistry of Low-Dimensional Materials, Huaiyin Normal University, Huaian 223300, China*
[4]*Department of Physics, Hong Kong University of Science and Technology, Clear water bay, Hong Kong, China*
[5]*Department of Materials Science and Metallurgy, University of Cambridge, Cambridge, United Kingdom*
[6]*Department of Nuclear Science and Engineering and Department of Materials Science and Engineering, Massachusetts Institute of Technology, Cambridge, Massachusetts 02139, USA*
[7]*City University of Hong Kong Shenzhen Research Institute, Shenzhen, China*
[8]*The Hong Kong Polytechnic University Shenzhen Research Institute, Shenzhen, China*

The formation, propagation, and structure of nanoscale cracks determine the failure mechanics of engineered materials. Herein, we have captured, with atomic resolution and in real time, unit cell-by-unit cell lattice-trapped cracking in two-dimensional (2D) rhenium disulfide (ReS_2) using *in situ* aberration corrected scanning transmission electron microscopy (STEM). Our real time observations of atomic configurations and corresponding strain fields in propagating cracks directly reveal the atomistic fracture mechanisms. The entirely brittle fracture with non-blunted crack tips as well as perfect healing of cracks have been observed. The mode I fracture toughness of 2D ReS_2 is measured. Our experiments have bridged the linear elastic deformation zone and the ultimate nm-sized nonlinear deformation zone inside the crack tip. The dynamics of fracture has been explained by the atomic lattice trapping model. The direct visualization on the strain field in the ongoing crack tips and the gained insights of discrete bond breaking or healing in cracks will facilitate deeper insights into how atoms are able to withstand exceptionally large strains at the crack tips.

The fundamental limitation in designing fracture resistant materials using elastic stress analysis is the presence of cracks that increase the local stresses near crack tips—causing real components to fail at much lower stresses than in ideal specimens. Despite decades of study, atomic structures of propagating crack tips (when loaded close to or over the Griffith load) in crystals have not been experimentally observed, and atomic resolution imaging of the crack tip and its propagation have remained elusive [1]. This has led to notable discrepancies between theoretical models and experiments [2–8]. While some controlled (referred to as stopped) cracks have been imaged in transmission electron microscopy (TEM) [9,10], and some mesoscopic fracture tests [11,12] and high resolution TEM observations [13,14]

on the atomically blunted crack tip zones were reported recently, the atomic structure of crack tips—whether they are atomically sharp or blunt [15–18]—in brittle materials remains unresolved. In particular, electron beam damage was present and the stress field in the crack tip zone has been released in previous TEM studies [13,14], which preclude further analysis on the intrinsic mechanical properties.

On the other hand, while theoretical calculations describe far field stress in front of or behind the crack tips, they are less successful in describing the divergent stress field near the crack tip because the atomic cohesive forces are well beyond the linear elastic regime but still provide bonding across the crack faces. Atomistic simulations of crack tips [5–8,19,20] require details of interatomic forces, which could be obtained experimentally. Regarding crack dynamics, a number of atomic-scale theories [21–23] have been established, however, without experimental verifications at the atomic scale. Many macroscopic experiments have revealed large discrepancies between the cracks in real brittle materials and the dynamical fracture theories, suggesting there are still unknown mechanisms [24].

The central difficulty in experimental real time capture of atomic structure of a fast propagating crack is the tradeoff between spatial and temporal resolution, as well as the control of the electron beam effect. Here we show that cracks in 2D materials [25] provide the ideal platform for studying fundamentals of cracks with atomic resolutions using *in situ* STEM. The ultrahigh flexibility and lattice switching capability of 2D ReS$_2$ membranes allows for the angstrom-scale displacement control of the vicinity of ongoing crack tip zone. Moreover, using the beam scanning mode, the cracking events were able to be analyzed either without or with the beam effect.

Anisotropic monolayered 2D ReS$_2$ [26] [Fig. 1(a)] was used to understand the structure of the crack tip and its propagation behavior at the atomic scale. The 2D samples were grown by the chemical vapor deposition (CVD) method (Supplemental Material [27], Fig. S1), and prior to the *in situ* STEM experiments, the defectless nature of our specimens have been first confirmed by the atomic force microscopy (AFM) indentation tests, the nearly ideal strengths have been demonstrated (Supplemental Material [27], Figs. S2–S4). Further, the 2D ReS$_2$ samples were transferred into Cs-corrected TEM (JEOL, ARM 200F) working under 60 kV at room temperature. Intensive

electron beam irradiation in TEM mode was initially used to generate large cracks on the sample (Supplemental Material [27]), which naturally led to several subcracks extending outside of the beam irradiation area [Fig. 1(b)], hence the these subcrack positions for *in situ* observations did not suffer from the intensive beam irradiation in the beginning. The following *in situ* STEM imaging condition was carefully controlled to avoid knockout damage on the sample (Fig. S5 [27]).

We then focused on the further cracking processes using STEM. The mode I crack—which occurs when tensile load is applied perpendicular to the crack direction—was most commonly observed. ReS$_2$ crystal is able to switch the crystal lattice directions (between *a* and *b*) under shear strain. Noted that the lattices of ReS$_2$ were switched in the postcrack edges [Fig. 1(c)], there is one tensile stress enhanced zone close to the crack tip zone due to the lattice expansion by the switched areas [inset of Fig. 1(c)], and it led to a tensile opening stress for mode I fracture on the crack tip zone [Fig. 1(c) and Fig. S6 [27]]. Two snapshots of such a mode I crack tip along the *a* axis of ReS$_2$, acquired through high angle annular dark field (HAADF) imaging are shown in Fig. 1(d). Wiener filtering was applied on HAADF images for reduction of noises. The
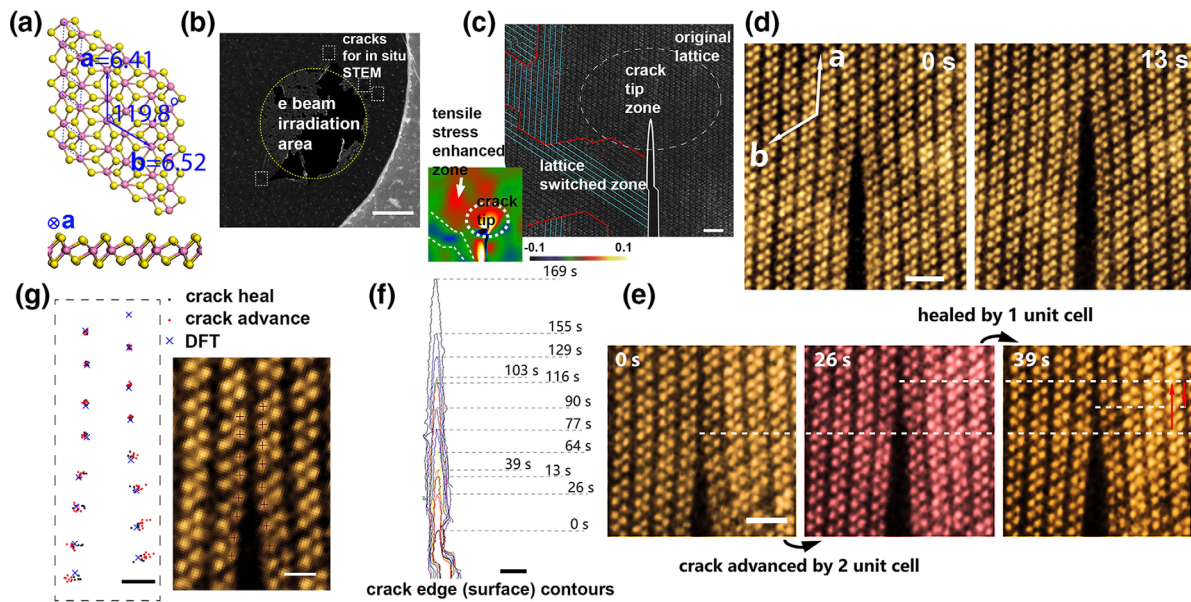

FIG. 1. The mode I cracks in 2D ReS$_2$ along the *a* axis. (a) The monoclinic crystal structure model of 2D monolayer ReS$_2$, plan view (upper) and side view (lower), with *a*,*b* as basis vectors. (b) The generation of initial cracks by *e* beam irradiation. Scale bar = 100 nm. (c) HAADF showing the mode I crack driven by postedge lattice switching. Scale bar = 2 nm. Inset shows the GPA strain analysis of this area for normal stress perpendicular to the crack direction. (d) Two HAADF snapshots of the crack tip zone of an ongoing crack. Crystal directions are highlighted by arrows. These directions apply to all of the HAADF images in Fig. 1. All images have been drift compensated and aligned to show the same positions of the specimen. False colors are applied on HAADF images. Brighter spots represent positions of Re atoms, while S atoms are barely visible. Scale bar = 1 nm. (e) *In situ* snapshot series of cracking and healing processes in 2D ReS$_2$ by single steps (unit cell). Cracking in yellow and healing in red. Scale bar = 1 nm. (f) Evolution of a crack edge contour observed by *in situ* STEM with observation times marked, scale bar = 2 nm. (g) The inner most 16 Re atomic positions inside the crack tips extracted from 13 experimental images (black: crack heal; red: crack advance), an example HAADF image shown in the right side, and the DFT simulation results are shown as blue crosses. All sets of atomic position data are aligned using the upper right Re atom's position as reference. Scale bar = 0.2 nm.

crack was straight and atomically smooth. We find that continuous cracking is discretized down to the atomic scale. That is, cracking is periodic and repeatable along the unit cells. Further observations suggest that both crack advance and crack healing can occur [Fig. 1(e)]. The continuous propagation of one crack tip (outline edge contours) in our experiments is depicted in Fig. 1(f).

Although fracture is usually irreversible, we were able to observe crack healing by rebonding of free edges behind the crack front [26 to 39 s in Fig. 1(e)]. The maximum length of continuous crack healing extends three unit cells in our observations (Fig. S7 [27]). The healing implies that the fracture is entirely brittle, and plasticity or reconstructions are absent in the ReS_2. The inner most Re atom positions within the crack tip zones were extracted from experimental images and overlaid with our density functional theory (DFT) analysis [28] results [Fig. 1(g)]. The experimental atomic positions for crack advance and healing were distinctly separated, in agreement with the DFT simulated atomic structures. Our DFT analysis results [Fig. 2(a) and Fig. S8 [27]] on mode I cracks along the *a* axis in ReS_2 also reproduce the atomically smooth edges and the sequential rupture and healing of Re-S bonding at the crack tips, depending on the initial strain applied. The free edges formed due to cracking were occupied by dangling S atoms, suggesting that there was neither knock-out of atoms by electron beam nor loss of atom during fracture process [Fig. 2(b) and Fig. S9 [27]]. The sequential *in situ* STEM observations sometimes captured the discontinuous lines in the images [Fig. 2(c)], which we will discuss in detail in the dynamic analysis below.

The strain fields near tip zone were mapped (Fig. S10 [27]) through the geometric phase analysis (GPA) [29] on the HAADF images. Meanwhile, utilizing the experimentally determined atomic structure of crack tips, the atomic strains were quantitatively analyzed for each half unit cell or Voronoi cell [30] to study the critical condition for crack advance (growth) or healing. In Fig. 2(d), crack heal
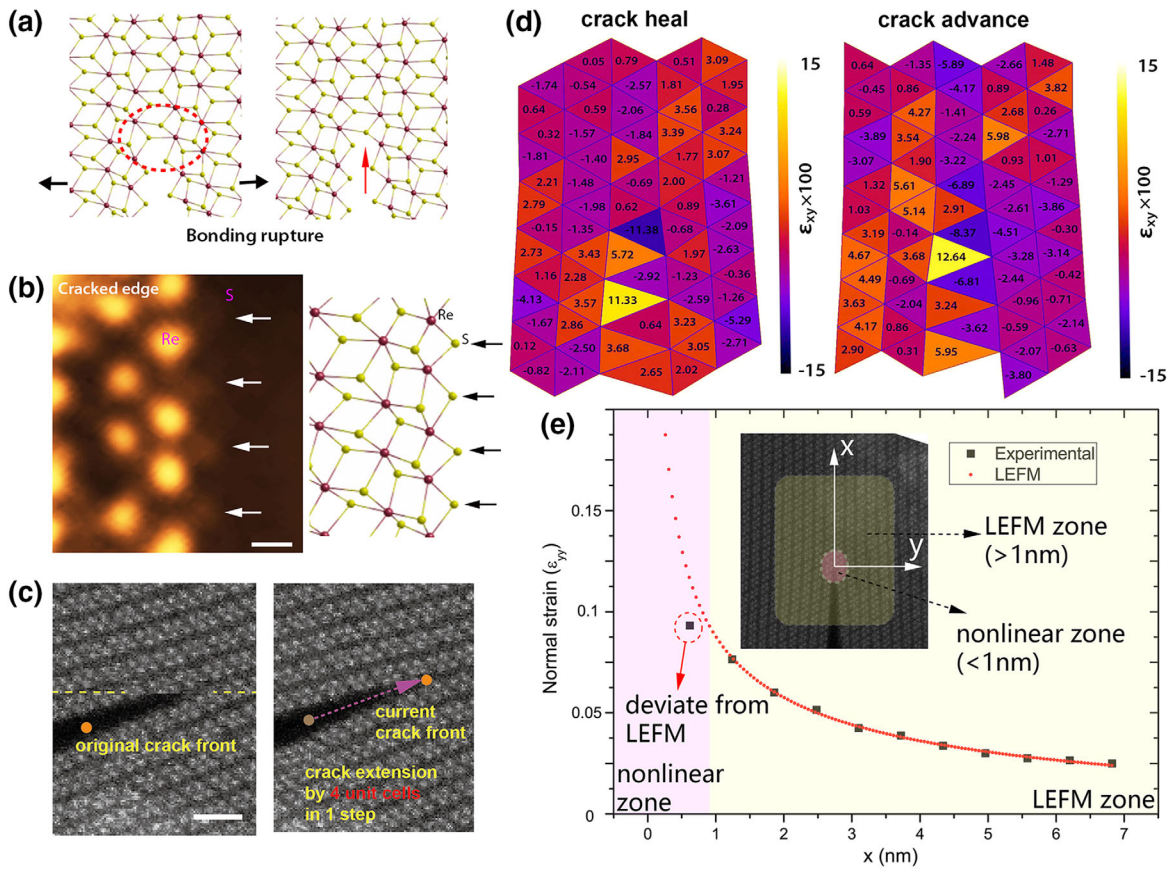

FIG. 2. Atomic-scale strain analysis on the crack tip zones. (a) Two sequential snapshots of DFT simulated mode I cracks in ReS_2. The ruptured Re-S bond is marked by red arrow. (b) Magnified HAADF image of one ReS_2 cracked edge, white arrows indicate the position of dangling S atoms. Scale bar = 0.3 nm. Corresponding DFT results of ReS_2 cracked edge shown on right side. (c) The discontinuity in STEM image caused by crack move when the electron beam is scanning closely to the crack tip. Two consecutive STEM snapshots of the same position in monolayer ReS_2 sample showing the crack instantly move by 4 unit cells when the beam scanning reaches the yellow dashed line position. Scale bar = 1 nm. (d) Shear strain results (color encoded, discretized by half unit cell) of ReS_2 Mode I crack and healing along the *a* axis in our experiments. (e) The normal strain on the *x* axis (shown in the inset) for mode I crack in 1L ReS_2. The strain inside the 1 nm region deviate from the LEFM theory.
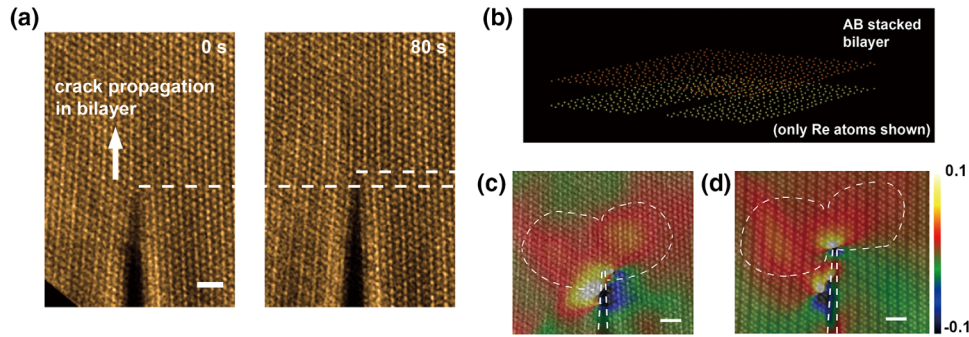
FIG. 3. Cracks in bilayers. (a) The STEM snapshots of a crack in bilayer (2L) ReS$_2$ which propagate by one unit cell. Scale bar = 1 nm. (b) Scheme for the bilayer ReS$_2$ and the always synchronized cracking in the upper and lower layers. (c) The normal (tensile) strain (e_{yy}) distribution corresponding to (a). Scale bar = 1 nm. (d) The normal strain distribution (e_{yy}) for another 1L ReS$_2$ sample, showing similar strain fields for 1L and 2L specimens. Scale bar = 1 nm.

and crack advance are two example snapshots taken in our experiment and here we show the lattice discrete strain analysis results on these STEM snapshots. The lattice discrete strain is calculated by the atomic displacement directly measured from STEM images. The formulation of the lattice discrete strain analysis (Fig. S11 [27]) and detailed analysis methods are introduced in the Supplemental Material [27]. According to the obtained atomic strains, in the range of 1–5 nm away from the crack tips, the asymptotic strain field by the linear elastic fracture mechanics (LEFM) [31,32] [Fig. 2(e) and Fig. S12 [27]] and the J integral approach [33] (Fig. S13 [27]) still hold, showing the fracture process induced a well-defined mode I crack. For the area out of the 1 nm tip zone, the LEFM relationship $\varepsilon_{yy}E = K(2\pi x)^{-1/2}$ can still be used to describe our experimental results [Fig. 2(e)], E is modulus. The stress intensity factor (K_I) is derived from the fitting parameter in the LEFM zone. For the area within the 1 nm tip zone, the strain field deviates from the LEFM and the J integral theory, while nonlinear deformation dominates.

We carried out similar experiments on bilayer ReS$_2$. For the commensurately stacked bilayer ReS$_2$ samples, the *in situ* TEM observed cracking in both layers are synchronized, which yield similar atomically sharp tips as monolayer ReS$_2$ [Figs. 3(a), 3(b)], the strain distributions are almost identical for the crack tips in bilayers and monolayers [Figs. 3(c), 3(d)]. In contrast, the incommensurately stacked bilayer ReS$_2$ could have roughened crack surfaces and different crack paths or directions in the two layers (Fig. S14, S15 [27]). Therefore, our cracking experiments directly exhibit the effect of interlayer vdW interactions. With stronger interactions (commensurate stacking), the basal plane strains can be transmitted through different layers, while under weak interaction (incommensurate stacking) the basal plane strains will have less correlation.

The macroscopic fracture criterion has been well established in the classical fracture mechanics [31,32]. However, in reality the loading required for fracture needs to exceed

the Griffith load (when the strain energy equals to the new surface energy). Here our experiments have confirmed the LEFM can be applied until very small regions (nm sized) within the crack tip for entirely brittle materials, and the stress intensity factor (K) can be obtained by fitting the strain distributions with LEFM theory [Fig. 2(e), and Fig. S12 [27]]. The statistics on all the *in situ* observations on the mode I cracks give the result shown in Fig. 4(a). Suggested by the fact that both cracking and healing have been observed, the K_I throughout our experiments is not surprisingly distributed close to the Griffith load [31]. The healing is induced by the stress intensity lower than the fracture toughness. Therefore, by our method the Griffith load (the mode I fracture toughness) can be determined. Applying the 2D modulus (E) directly measured by our AFM indentation experiments (Supplemental Material [27]), the mode I fracture toughness of 1L ReS$_2$ is determined as 2.5 ± 0.2 MPa m$^{1/2}$. Moreover, close to the Griffith load, the dynamics of the cracking is governed by the lattice-trapping energy barriers [22,23], which means the thermal energy is required to activate the cracking events. The lattice trapping barrier heights are controlled by the crack stress intensity. When the lattice trapping barriers for healing are lower than the barriers for crack advance, healing will occur.

By our serial *in situ* STEM imaging, the electron beam effects can be either included or excluded in the *in situ* crack tests. Two types of crack dynamics have been observed. One type is the cracking event when the electron beam scanning is over or close to the crack tip zone, in this case a discontinuous scanning line will appear in the image and we can measure the cracking length (defined as one step) during *ca.* 10 ms (19 μs × 512 pixels in one scanning line) [Fig. 2(c) and Fig. S16 [27]]. On the other hand, we also found in some serial STEM snapshots, the discontinuous lines as above are totally absent, however the cracks still propagated a few unit cells known from the two successive STEM snapshots before and after the crack moves. In these cases, the crack move events should occur
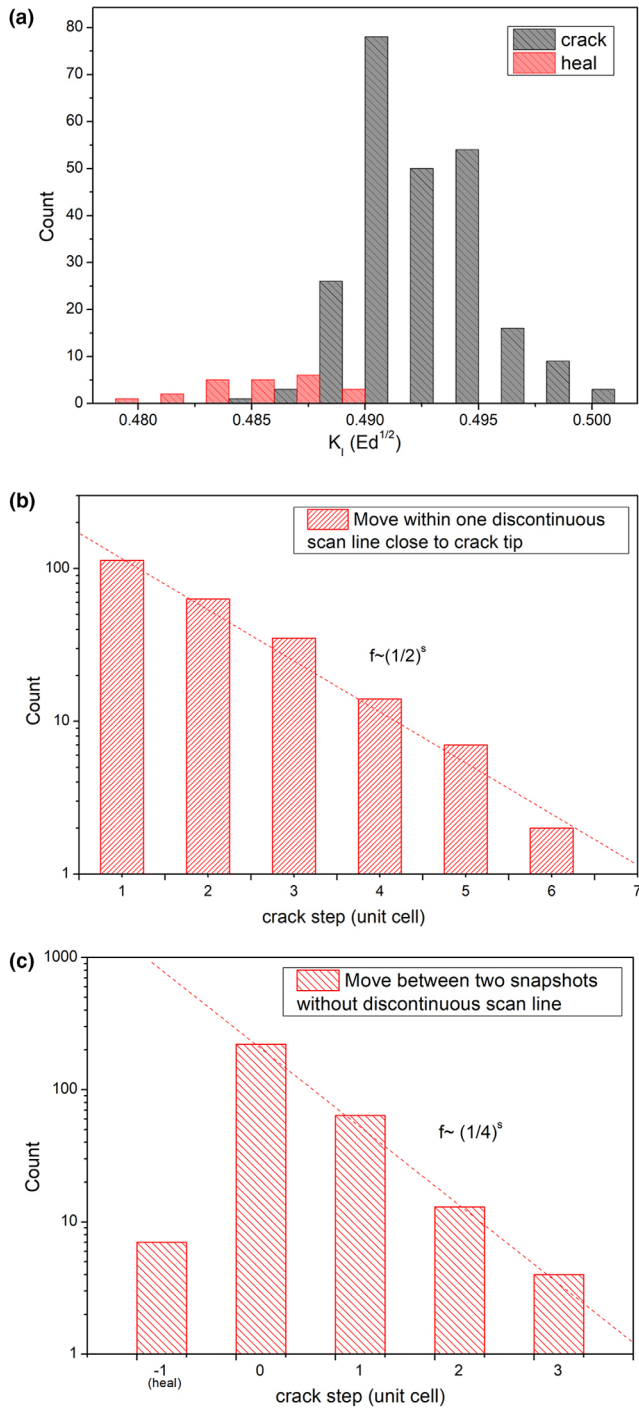
FIG. 4. The statistical results on the mode I crack and crack dynamics in $1L$ ReS$_2$. (a) The histogram on the frequencies of loaded stress intensity (K_I) for our experimental mode I crack moves, crack advance, and crack heal cases are distinguished. E is modulus of and d is the lattice spacing perpendicular to cracking (y) direction for ReS$_2$. (b) The histogram for frequencies of crack moving lengths (step) within one line scan of electron beam ($\sim$10 ms), so it means the electron beam is close to the crack tip when crack moves. (c) The histogram for frequencies of crack moving lengths between two continuous snapshots of STEM images ($\sim$5 s) when the electron beam is far away from the crack tip and no discontinuous lines are observed.

when the electron beam is scanning over other areas on the sample with very small atomic displacements upon the crack moves, which are far from the crack tip zone (>5 nm distances to the tip), therefore the electron beam should have negligible effects on these crack moves. In this sense, by snapshots with or without discontinuous scanning lines, we can include or exclude the electron beam effects in our following dynamic analysis. The experimental statistical results on the observed frequencies (f) versus crack move lengths (s) for these two cases are presented in Figs. 4(b), 4(c), respectively.

In both cases, the frequencies have exponential decay on the crack move lengths, in agreement with the lattice-trapped crack model. The crack propagation can be discretized down to individual moves (each single chemical bonding rupture) trapped by certain energy barriers. As the loading in our *in situ* experiments is controlled very close to Griffith load [Fig. 4(a)], the lattice trapping barriers can be considered as constant. Thus the frequencies of crack lengths should follow $f \sim z^s$ (see Supplemental Material [27] for details of modeling), where $z = \nu(\tau/6)\exp(\Delta E/kT)$, ν is the vibration frequency and τ is the time interval for STEM snapshots. Using the experimentally obtained z values in Fig. 4(c) and ν estimated by average phonon frequencies, the energy barrier for lattice trapping model without electron beam effect can be determined as 0.78 eV. As there are four times of bonding ruptures in one crack propagating over one unit cell in $1L$ ReS$_2$, four sub-barrier heights in one unit cell obtained by the DFT simulation are between 0.4 to 0.8 eV (Fig. S17 [27]). Since 0.8 eV is quite close to our experimentally obtained 0.78 eV, our experiments here suggested the lattice trapping barrier should be mainly attributed to the highest sub-barrier.

Further, applying this barrier height for analyzing the data in Fig. 4(b), the effective temperature of the lattice affected by electron beam can be estimated as 374 K, which means the effective lattice temperature of crack tip due to beam scanning right on the crack tip has been raised by around 76 K (a combined effect of knock-on and radiolysis). Using the heat dissipation model in two dimensions, the region close to the scanning beam (within 1 nm) can experience an over fivefold temperature rise than the region far away from the beam (>5 nm), hence the beam effect on the crack tip when electron beam is out of the 5 nm crack tip zone is negligible (temperature rise less than 10 K), and the intrinsic lattice-trapped barrier without irradiation damage (atomic sputtering or bonding dissociation) is confirmed.

Our *in situ* STEM observations have experimentally unveiled the atomic structures of propagating lattice-trapped crack tips. We observed entirely brittle fracture down to the atomic scale without tip blunting in 2D ReS$_2$. The fracture toughness and lattice-trapping energies for cracks are measured by our direct atomic-scale imaging. We have experimentally demonstrated that, beyond the

asymptotic field description in classical theories, the atomistic process in the singular crack tip zone is basically the sequential atomic bonding dissociation assisted by thermal energy. Since the lattice trapping barrier is highest for the Griffith load, and can be reduced by the increased loading or even totally vanish above the athermal loading, it is essential to maintain the experimental condition close to the Griffith load to achieve the high-resolution atomic scale imaging of the propagating crack tips. In short, our work has opened new avenues to explore the atomistic fracture mechanisms.

---

[*]These authors contributed equally to this work.
[†]thuchly@cityu.edu.hk
[‡]jiongzhao@polyu.edu.hk

[1] E. Bitzek, J. R. Kermode, and P. Gumbsch, Int. J. Fract. **191,** 13 (2015).
[2] J. Cook and J. E. Gordon, Proc. R. Soc. Lond. A **282,** 508 (1964).
[3] J. R. Rice and R. Thomson, Philos. Mag. A **29,** 73 (1974).
[4] J. W. Hutchinson, J. Mech. Phys. Solids **16,** 13 (1968).
[5] F. F. Abraham, D. Brodbeck, R. A. Rafey, and W. E. Rudge, Phys. Rev. Lett. **73,** 272 (1994).
[6] J. A. Hauch, D. Holland, M. P. Marder, and H. L. Swinney, Phys. Rev. Lett. **82,** 3823 (1999).
[7] Z. Zhang, A. Kutana, and B. I. Yakobson, Nanoscale **7,** 2716 (2015).
[8] S. S. Terdalkar, S. Huang, H. Yuan, J. J. Rencis, T. Zhu, and S. Zhang, Chem. Phys. Lett. **494,** 218 (2010).
[9] D. R. Clarke and K. T. Faber, J. Phys. Chem. Solids **48,** 1115 (1987).
[10] B. R. Lawn, B. J. Hockey, and S. M. Wiederhorn, J. Mater. Sci. **15,** 1207 (1980).
[11] C. Lee, X. Wei, J. W. Kysar, and J. Hone, Science **321,** 385 (2008).
[12] P. Zhang, L. Ma, F. Fan, Z. Zeng, C. Peng, P. E. Loya et al., Nat. Commun. **5,** 3782 (2014).
[13] T. H. Ly, J. Zhao, M. O. Cichocka, L. J. Li, and Y. H. Lee, Nat. Commun. **8,** 14116 (2017).
[14] S. Wang, Z. Qin, G. S. Jung, F. J. Martin-Martinez, K. Zhang, M. J. Buehler, and J. H. Warner ACS Nano **10,** 9831 (2016).
[15] B. R. Lawn, K. Jakus, and A. C. Gonzalez, J. Am. Ceram. Soc. **68,** 25 (1985).
[16] S. Ito and M. Tomozawa, J. Am. Ceram. Soc. **65,** 368 (1982).
[17] C. Cao, S. Mukherjee, J. Y. Howe, D. D. Perovic, Y. Sun, C. V. Singh, and T. Filleter, Sci. Adv. **4,** eaao7202 (2018).
[18] S. Kondo, A. Ishihara, E. Tochigi, N. Shibata, and Y. Ikuhara, Nat. Commun. **10,** 2112 (2019).
[19] J. G. Swadener, M. I. Baskes, and M. Nastasi, Phys. Rev. Lett. **89,** 085503 (2002).
[20] D. Holland and M. Marder, Phys. Rev. Lett. **80,** 746 (1998).
[21] H. Tan and W. Yang, Int. J. Fract. **77,** 199 (1996).
[22] R. Thomson, C. Hsieh, and V. Rana. J. Appl. Phys. **42,** 3154 (1971).
[23] T. Zhu, J. Li, and S. Yip, Proc. R. Soc. A **462,** 1741 (2006).
[24] M. J. Buehler, H. Tang, A. C. T. van Duin, and W. A. Goddard III, Phys. Rev. Lett. **99,** 165502 (2007).
[25] M. Chhowalla, H. S. Shin, G. Eda, L.-J. Li, K. P. Loh, and H. Zhang Nat. Chem. **5,** 263 (2013).
[26] Y. C. Lin et al. ACS Nano **9,** 11249 (2015).
[27] See Supplemental Material at http://link.aps.org/supplemental/10.1103/PhysRevLett.125.246102 for experimental details, notes and supplementary data.
[28] G. Kresse and J. Furthmuller, Phys. Rev. B **54,** 11169 (1996).
[29] J. L. Rouviere and E. Sarigiannidou, Ultramicroscopy **106,** 1 (2005).
[30] J. S. Ferenc and Z. Néda, Physica (Amsterdam) **385A,** 518 (2007).
[31] A. A. Griffith VI., Phil. Trans. R. Soc. A **221,** 163 (1921).
[32] G. R. Irwin, Proc. 7th Sagamore Res. Conf. (1961), Vol. 4, p. 63.
[33] J. R. Rice, J. Appl. Mech. **35,** 379 (1968).

Supplemental Material for

In situ **scanning transmission electron microscopy observations of fracture at the atomic scale**

Lingli Huang[1+], Fangyuan Zheng[2+], Qingming Deng[3+], Quoc Huy Thi[1+], Lok Wing Wong[2], Yuan Cai[4], Ning Wang[4], Chun-Sing Lee[1], Shu Ping Lau[2], Manish Chhowalla[5], Ju Li[6], Thuc Hue Ly[1,7*], Jiong Zhao[2,8*]

[1] Department of Chemistry and Center of Super-Diamond & Advanced Films (COSDAF), City University of Hong Kong, Kowloon, Hong Kong, China.

[2] Department of Applied Physics, The Hong Kong Polytechnic University, Kowloon, Hong Kong, China.

[3] Physics department and Jiangsu Key Laboratory for Chemistry of Low-Dimensional Materials, Huaiyin Normal University, Huaian 223300, China.

[4] Department of Physics, Hong Kong University of Science and Technology, Clear water bay, Hong Kong, China.

[5] Department of Materials Science and Metallurgy, University of Cambridge, UK

[6] Department of Nuclear Science and Engineering and Department of Materials Science and Engineering, Massachusetts Institute of Technology, Cambridge, Massachusetts 02139, United States

[7] City University of Hong Kong Shenzhen Research Institute, Shenzhen, China.

[8] The Hong Kong Polytechnic University Shenzhen Research Institute, Shenzhen, China

This material includes Supplemental Notes and Supplemental FIGs. S1-S17.

Supplemental Notes

Synthesis of Rhenium Disulfide (ReS$_2$)

ReS$_2$ was grown on a c-face sapphire substrate by the atmospheric CVD system. Ammonium perrhenate (NH$_4$ReO$_4$) (Aldrich, 99.999 %) and Sulfur powder (Aldrich, 99.998 %) were used as precursors with weight ratio 1: 50, separately put in two quartz boats. The clean c-face sapphire 1 cm × 1 cm substrate was placed polished face down on the top of Re source. A two-zone splitting tube furnace was used to control accurately Sulfur and substrate zone temperature, respectively. Prior to the temperature ramping up, 300 sccm of Argon gas was purged through the quartz tube for 10 minutes. During the deposition process, argon gas (80 sccm) was as the carrier gas to transport sulfur vapor to substrate zone. The sulfur zone was ramped to 200 ° C, at the same time, the substrate zone reaching 850 ° C in 30 minutes and then held for 10 minutes. The stable T$_d$ phase in ambient condition of ReS$_2$ is triclinic and highly anisotropic, which stems from the tetragonal (T) phase prevalent in transition metal dichalcogenides (TMDs) with "diamond" type superlattices in two directions (labeled as *a* and *b*) and slightly distorted (γ=119.8°). *Supplemental Material* FIG. S1 shows the major characterization results of our mono-atomic-layer ReS$_2$ membrane. The bilayer ReS$_2$ specimens were prepared by the same methods and in some flakes commensurately or incommensurately stacked bilayer ReS$_2$ could be found.

(S)TEM specimen preparation

By PMMA-assisted technique, the CVD grown ReS$_2$ was transferred on a TEM grid. Initially, thin layer PMMA was spin coated on the as-grown sapphire substrate at 3000 rpm for 50 seconds. With the aid of PMMA, the ReS$_2$ detached from substrate by emerging in 75 ° C deionized water for two hours. Next, the PMMA/ ReS$_2$ layer was transferred onto a TEM grid and dried at ambient temperature. Acetone vapor was introduced for gentle removal of PMMA film.

(S)TEM characterizations

Different from previous studies which applied the continuous beam exposure during TEM imaging [13,14], the aberration corrected STEM under 60 kV accelerating voltage was applied in this work to prevent beam damage. The 60 kV operation can significantly reduce the knock-on damage for S and Re atoms in monolayer ReS$_2$. Moreover, the ultrafine displacement control of the crack front down to single unit cell scale was achieved. These technical improvements are key to the realization of the atomistic crack observations. In specific, the STEM images for ReS$_2$ samples were performed on a JEM-ARM200F transmission electron microscope (TEM) retrofitted with a CEOS spherical (Cs) aberration corrector. A vacuum value during measurement was 1.3×10^{-7} mbar, together with the electron beam current of 13 pA. At the time of performance, the scanning probe size was 1.5 Å. For image acquisition, the camera length of STEM was 120 mm. The defocus was -4 nm and acquisition time of HAADF image was 19 μs per pixel in order to minimize damage and get the FIG with lower drift. The 512 × 512 pixel

images were acquired with the CL aperture of 40 μm and the range of collection angle was 45 to 180 mrad so that the atomic images with proper contrast can be obtained. Wiener filtering was applied on HAADF images for reduction of noises.

In situ STEM on cracking

Ultrahigh beam intensities (spread beam with intensity over 0.3 pA/nm^2 usually for beam shower) were exposed on controlled circled areas (~100 nm diameter) of ReS$_2$ for 15~30 min. Afterwards the beam was quickly switched to STEM imaging on the crack dynamics outside of the beam exposed zones. These freshly generated cracks by such method can further extend 10~50 nm, depending on specific stress conditions. The particular lattice switching in ReS$_2$ layers also contribute to the in-plane mechanical loading. The time interval of serial *in situ* STEM imaging is between 1~20 s. The specimen drift was compensated, hence the dynamics of cracks could be directly registered. Lower magnification image is shown in FIG. S5a. The crack along the *a* axis was straight and atomically smooth. No loss of atoms or reconstruction was noticed at the cracking tips. Beam damage will be induced only if we change the STEM conditions (see *Supplemental Material* FIG. S5c). In addition, the exact time for each step of crack propagation could be determined by the discontinuous lines in images due to the crack front movement while electron beam scanning (see *Supplemental Material* FIG. S5b). However such movements close to the crack tip/front (see *Supplemental Material* FIG. S16) were less frequently seen, showing the crack tip movement is normally irrelevant to the electron beam excitations, but triggered by mechanical origins (see *Supplemental Material* FIG. S6).

We have also carried out *in situ* STEM fracture experiments on the bilayer ReS$_2$ specimens. Owning to the ultrathin sample thickness, the crack process (in the local crack tip zone) can be regarded as under in-plane stress condition. The fracture behavior and atomic fracture criteria measured in the AB stacked ReS$_2$ bilayers are quite similar to the results for monolayers (main text FIG. 3a). Hence the commensurately stacked vdW layered materials will have synchronized fracture process in all the layers, which means the results in mono-atomic layers can be generalized to thicker crystals. Due to the weak vdW bonding between the layers, the incommensurate stacked layers may follow different crack paths in atomic scale (*Supplemental Material* FIG. S14). The crack directions along the relatively favorable *a* axis and *b* axis (lower surface energy directions and cleavage planes) will compete with the driving force directions. Hence the atomically roughened surface can be yielded. Sometimes, the leading crack in one vdW layer will be arrested/stopped by the constraint from another vdW layer if the crack has not extended to that position yet (*Supplemental Material* FIG. S15). Overall, the incommensurate stacked membranes will have higher fracture toughness according to our observations.

Strain analysis on TEM images

The GPA strain analysis [28] (on high resolution HAADF images) was performed with the reflexes (in reciprocal space) perpendicular to *a* and *b* axis as the two basis, respectively. The

GPA analysis resolution was set as 0.3~0.4 nm, smoothing factor was set as 7.0.

More quantitatively, we applied the discretized atomic strain analysis on the HAADF images, considering the lattice structure and crystal symmetry in different materials, it was performed for half unit cells or Voronoi cells (for ReS_2, determined by the locations of Re retrieved by Gaussian fitting of STEM images after a ten times pixel interpolation in the images, to reduce noise on strain measurements, and neighboring four cells are averaged for further stress intensity measurement, see *Supplemental Material* FIG. S12). The coordination (*x* and *y*) of the discrete atomic stress, strains are defined along the *a* axis (y) and perpendicular direction of *a* axis (x). Their locations are defined by the averaged three corner positions of the triangular cells, and the faces are defined as the faces perpendicular to *x* and *y* coordinates, respectively. Non-deformed state (the zero stress/strain condition) is relaxed by DFT, corresponding to our high resolution STEM measurement results. The normal and shear strain components of the cells follow the standard of linear elastic mechanics (finite element theory) (assume the triangular cells have constant strain over the cell if the three corner positions (u_1, v_1; u_2, v_2; u_3, v_3)) are determined (by *in situ* STEM images) under linear approximation), see *Supplemental Material* FIG. S11. $\{\varepsilon_x, \varepsilon_y, \varepsilon_{xy}\} = \{\frac{\partial u}{\partial x}, \frac{\partial v}{\partial y}, \frac{\partial u}{\partial y} + \frac{\partial v}{\partial x}\}$. This formalism can be applied for all the cells in the lattices/images including the singular crack tip zone. Average strain values of four neighboring cells are taken for fitting with LEFM results (see *Supplemental Material* FIG. S12).

Clear strain mapping is needed to elucidate the origin of the crack extension/healing. Although our sample is not subjected to any external loading, the strain distribution (by GPA) in the nm-sized mode I, II and III crack tip zone shows the typical features as predicted from continuum LEFM theory (FIG. S9). The driving force and stress boundary condition for cracking is illustrated as in FIG. S10. In the range of 1~5 nm away from the crack tip zones, the asymptotic strain field by the LEFM (linear elastic fracture mechanics) and the J integral approach still hold. For the area within 1 nm to the crack tips, in Mode I crack, the strain fields deviate from the LEFM stress field as well as the J integral theory. In terms of atomic position, according to the snapshots taken by *in situ* STEM for mode I cracks, we have overlaid the extracted atomic positions for the inner most 16 Re atoms of the crack tips in one same FIG, and compare them with the DFT calculation results (main text FIG. 1g). For crack advance and crack healing, there is clearly a boundary, almost identical to the atomic positions given by the DFT calculations. The atomic strain (maximum strain gradient) in the <1 nm crack tip zone (by atomic strain analysis) is correlated with the stress intensity factor (K) estimated by the LEFM theory, and the J integral approach is also applied and yield similar results as LEFM theory (*Supplemental Material* FIG. S13). FIG. 2e in main text and FIG. S11 in *Supplemental Material* shows the stress components and directions. Therefore, in terms of driving force, the atomic scale (the nonlinear/linear deformation zone by discrete unit cell mapping) and the macroscopic scale (stress intensity factor K or the energy release rate J/G) are now bridged.

Density Functional Theory calculations

All atomistic calculations in this study were carried out by using spin-polarized density function theory (DFT) calculations as implemented in the Vienna ab initio simulation package (VASP) [27] program package to explore the geometries of ReS_2 monolayer. The exchange-correlation interactions are described by using PBE functional [33] with a gradient approximation (GGA) [34]. The kinetic energy cuto for the plane-wave basis set was 400 eV, and the electronic SCF tolerance was set to 10^{-4} eV. The distance of vacuum layer was set to be more than 15 Å, which was adequately large to avoid interlayer interactions. Fully relaxed geometries were obtained by optimizing all atomic positions until the Hellmann–Feynman forces are less than 0.05 eV/Å. The k-points samplings are 3×1×1 in the Brillouin zone for structural optimizations. The size of the DFT supercell is 2.74 nm width (*x* axis) by 4.00 nm length (*y* axis), and z direction is 15 Å which can provide enough space to avoid the interactions by layers. The system contains 80 Re atoms and 156 S atoms to simulate the entire fracture process. The uniaxial load is applied by elongating the length the supercells along x coordinate (perpendicular to the a axis in ReS_2). The strain, $\varepsilon = (c_s - c_0)/c_0$ corresponds to the applied stretching (6-10%), where c_s and c_0 are the lattice constant of strained and the pristine ReS_2 monolayer along *y* axis (crack direction). The pre-cracks were introduced by removal of four neighboring S atoms.

AFM indentation measurements

Force curves were experimental obtained using Atomic Force Microscope (AFM5300E, Hitachi, Japan) with a silicon probe (DF3P2, Hitachi). The prepared sample (ReS_2) was put suspended on the gap of a metal plate, and a needle-sharp silicon (Si) patterned substrate (TGT1, K-TEK) was placed next to it as a calibration sample. A quantitative analysis to measure the tip radius of probe, the spring constant of the cantilever and calibrate the sensitivity of detector to the Z direction displacement of cantilever (DIF sensitivity) was performed prior to the force measurement. After measuring/calibrating necessary parameters of the probe, topography of the prepared sample (ReS_2) was measured to find the suspended position. Note that the SIS mode was used to prevent the deformation of sample/tip. Finally, the probe was gradually moved against the suspended position from original surface level downward, and the corresponding interaction force between probe and sample was measured at the same time.

We have carried out the AFM indentation tests on the ReS_2 membranes as well as other 2D membranes using the similar approach as reported by literature (ref 11 of main text) (FIG. S2). Our setup and calibration of the AFM tip radius are shown in FIG. S3. The nearly ideal strength (1/8~1/10 of modulus) in ReS_2 was measured (FIG. S4), implying the original samples do not have notable defects, and the fracture observations on our ReS_2 samples can exhibit the intrinsic crack behavior. The experimental 2D modulus E_{2D} (~300 N/m) and maximum 2D strengths (~38 N/m) of ReS_2 monolayer can be therefore applied in the calculation of the stress intensity and fracture toughness. Note here the isotropic 2D indentation is assumed, although ReS_2 does have 2D in-plane elastic anisotropy (modulus: 191 and 200 GPa along two in-plane directions according to elastic stiffness matrix values [Materials Project id mp-572758]). The AFM measured modulus by us are close to the theoretical elastic properties of ReS_2. In conclusion, our

5

AFM indentation measurements have verified the defect-less nature as observed by the direct STEM atomic scale imaging.

The lattice trapping crack model

The lattice trapping model was first raised up in 1971 [22] and then developed further into three-dimensional [23]. Because of the discrete lattice, the energy landscape under loading below the athermal threshold is corrugated by periodic energy barriers. The conditions in our experiments are close to the Griffith load, hence cracks are governed by lattice trapping energies. The probability (p) for each move under thermal energy kT should be

$$p = v\tau\exp\left(\frac{\Delta E}{kT}\right),$$ (eq.1)

v is the vibrational frequency, τ is the time of observation, ΔE is the energy barrier height. If the probability for moving over s steps in the time interval τ is $P(s)$, then

$$P(s + 1) = \int_0^\tau P(s)\frac{\tau - t}{\tau}v\exp\left(\frac{\Delta E}{kT}\right)\frac{t}{\tau}dt = P(s)v\frac{\tau}{6}\exp\left(\frac{\Delta E}{kT}\right),$$ (eq.2)

The above has assumed the reverse-direction move (crack heal) has much lower probability than forward (crack). It is true for loading higher than the Griffith load. Finally, the experimentally observed frequency (f) for crack moving s steps in a time interval τ can be derived as

$$f(s) = P(s) - P(s + 1) = c(z)^s,$$ (eq.3)

where $c = 1 - v\frac{\tau}{6}\exp\left(\frac{\Delta E}{kT}\right)$, and $z = v\frac{\tau}{6}\exp\left(\frac{\Delta E}{kT}\right)$.

Accordingly, the frequencies should follow the exponential decay over the crack step lengths, as observed in our experiments.
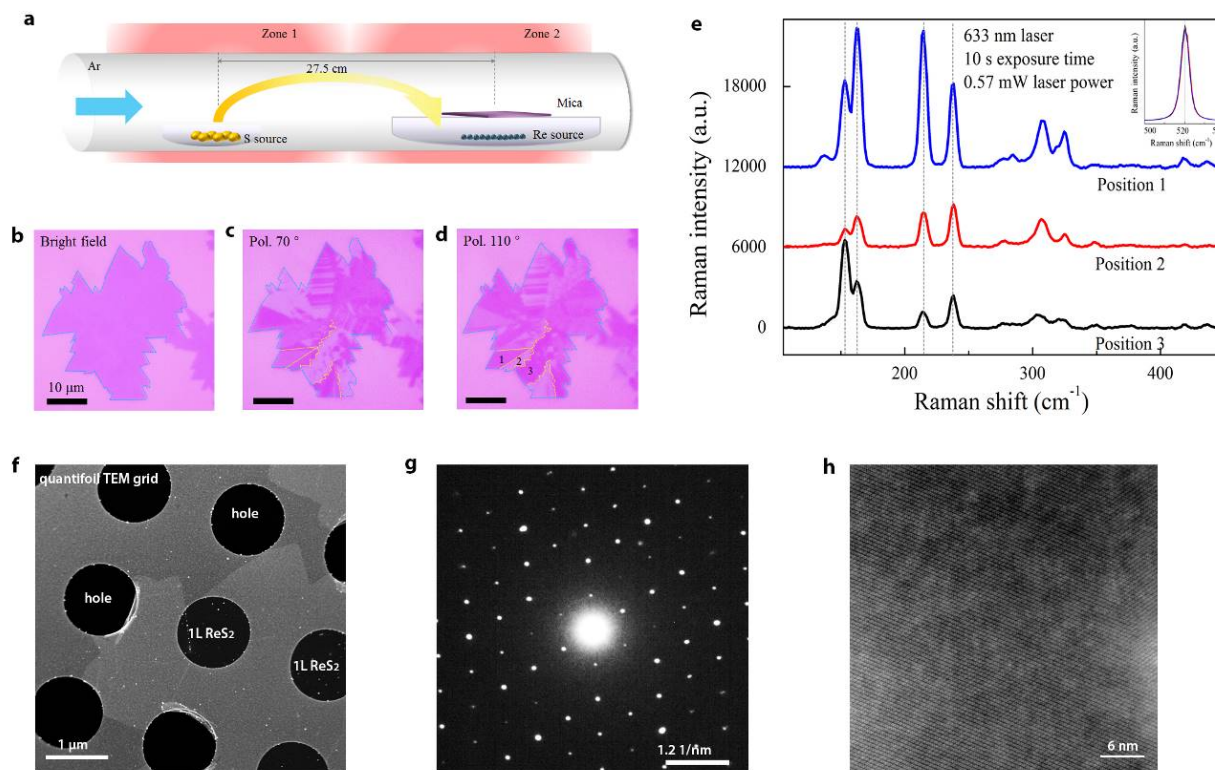
Supplement FIGs S1-S17

FIG. S1 The characterization results on CVD synthesized ReS_2. (a) Scheme showing the CVD process of ReS_2. (b-d) Optical microscopy images showing the size, morphology and domain structures of anisotropic monolayer ReS_2. Scale bars=10 μm. (e) The Raman spectra of monolayer (1L) ReS_2 corresponding to the Positions marked in (d). (f) Low magnification STEM image of transferred ReS_2 membrane on Quantifoil[TM] TEM grid. (g) Selected area diffraction (SAED) pattern of 1L ReS_2 single crystal. (h) HAADF image of pristine single crystal area of ReS_2 showing the good crystallinity.
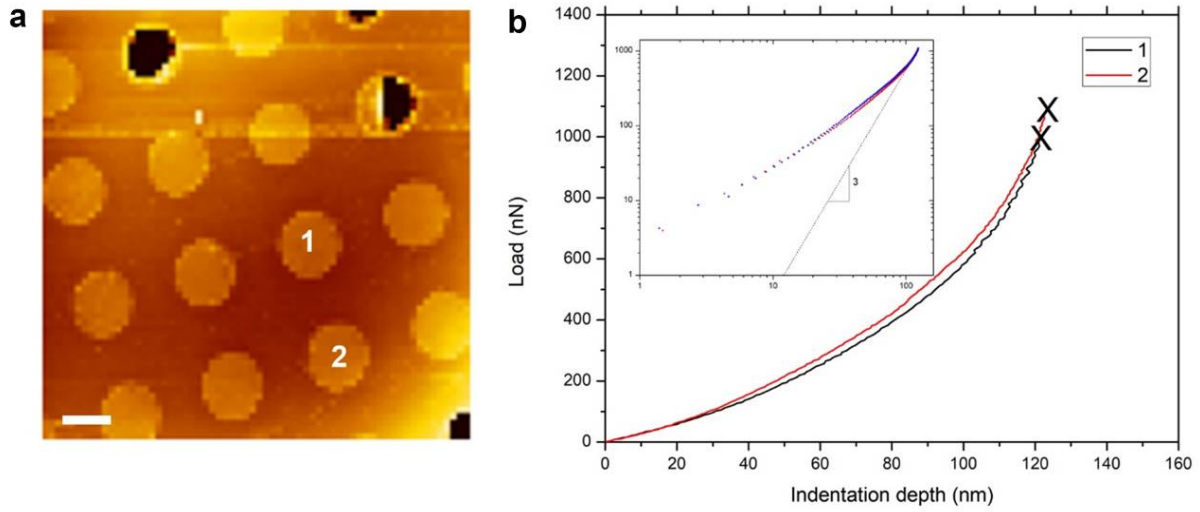
FIG. S2 The AFM indentation tests on the ReS$_2$ monolayer samples. (a) The AFM topography image for the sample conFIGuration. The circle hole arrays have diameters 1.2 μm. Scale bar = 1μm. (b) The F-d curves for the 1 and 2 position indentations of a, respectively. Inset shows the curves approaching cubic in high loads. The specimens usually have sudden failure (labeled by X) under around 1000 nN monotonic loading.
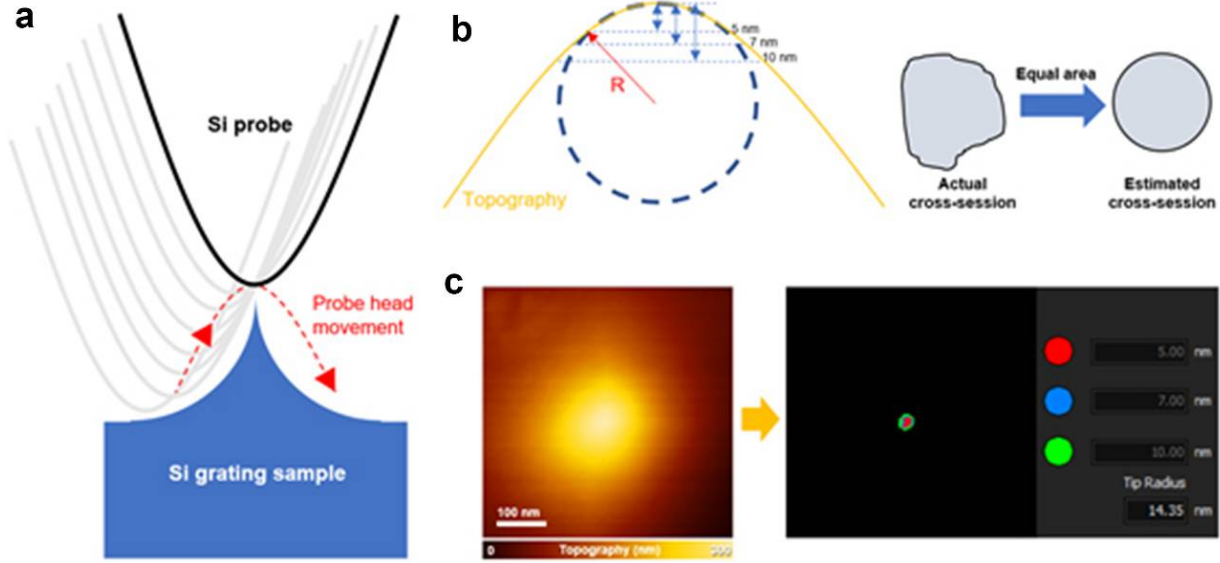
FIG. S3 The AFM tip radius calibration. (a) movement of the tip on grating pattern. (b) Schematic illustrates the tip estimation cross-sections from the result of tip movement (topography). (c) The cross-section area (right side) of 5-nm (red), 7-nm (blue) and 10-nm (green) were carried out from the topography image (left side), and tip radius of 14.35 nm was calculated. For measuring tip radius, the probe was approached onto the needle-sharp Si patterned substrate to observe the topography using the sampling intelligent scan (SIS) mode. Since the Si needle pattern was sharper than the tip head, the topography visualized sharpness of the tip itself (FIG. S3a). The tip radius was calculated from the cross-section approximation at 5 nm, 7 nm and 10 nm distance from the top height of topography image. Note that the actual non-circular sharp cross-sessions were converted to the estimated circular sharp cross-sessions with equal area (FIG. S3b,c). The evaluation process revealed that the tip radius of original DF3P2 probe had value of 10 – 15 nm. Next, thermal vibration of cantilever was detected using the optical lever detection system installed in the instrument. The spring constant of a cantilever oscillating slightly due to thermal vibration was calculated by following equation,

$$K = \frac{0.971 \times k_B \times T}{\chi^2 \langle z^{*2} \rangle}$$

Where K is the cantilever spring constant, k_B is Boltzmann constant, T is absolute temperature, χ^2 is the correction factor and $\langle z^{*2} \rangle$ is the mean square of displacement in the Z direction measured with the optical lever system. Subsequently, the probe was pressed against the ideal rigid plane (silicon substrate). The bending level of cantilever with related pressing force were used to calibrate DIF sensitivity. The DF3P2 probe had optimized DIF sensitivity value of 11 – 13 mV/nm.
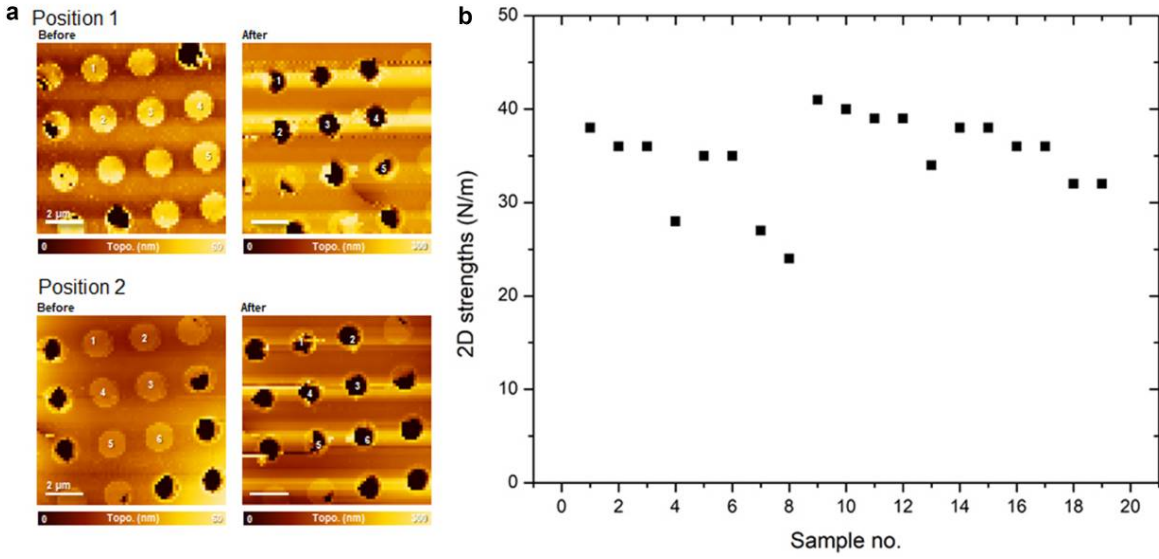
FIG. S4 The AFM indentation results. (a) AFM topographic images of ReS$_2$ monolayer samples before and after indentation. (b) 2D strengths of 19 representative 1L ReS$_2$ samples, showing the stable strengths originated from the good quality and defect-less of original specimens.
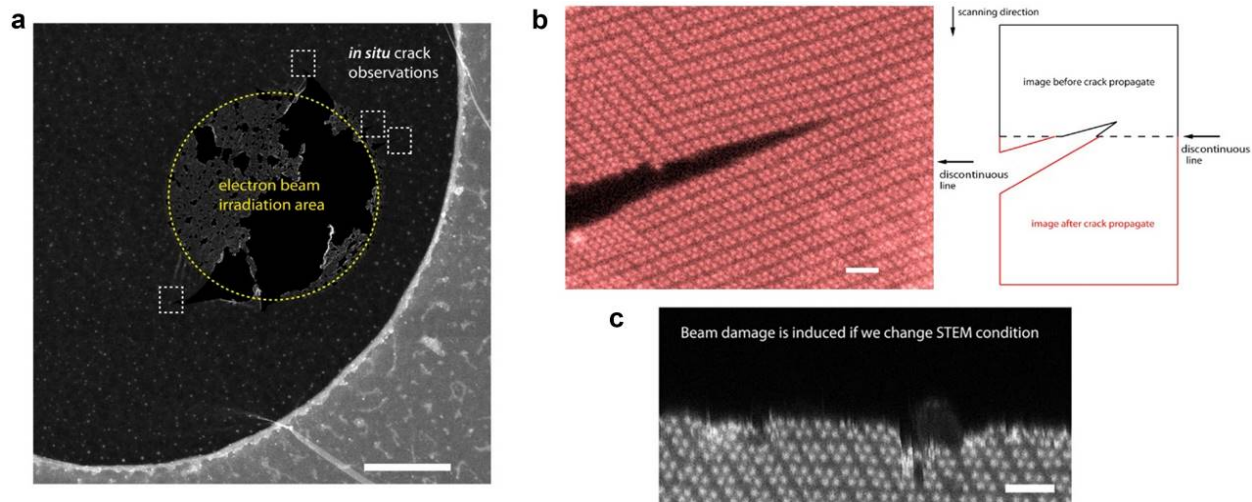
FIG. S5 The *in situ* cracking method and conditions. (a) Low magnification image of 1L ReS$_2$ after controlled beam irradiation in circled area, several cracks are formed and left for higher magnification imaging, these observation areas (dashed rectangles) are without any prior electron beam irradiation. Scale bar 100 nm. (b) The crack propagation occurs when the scanning (of STEM) reached the discontinuous line (left panel), close to the crack tip zone, scale bar=1nm. In the other case, the discontinuous line cannot be seen if the crack move occurs when the electron beam is far away (>5 nm) from the crack tip zone. This is because the movement of atoms is negligible except the atoms in the crack tip zone during the propagation of crack over one or few unit cell. In the statistical results (FIG. 4b,c), the cases with discontinuous line and without discontinuous line are separated and correspond to conditions with electron beam effect and without electron beam effect, respectively. (c) The HAADF image of beam damaged edges if the scanning time for each pixel is doubled. Scale bar 1 nm.
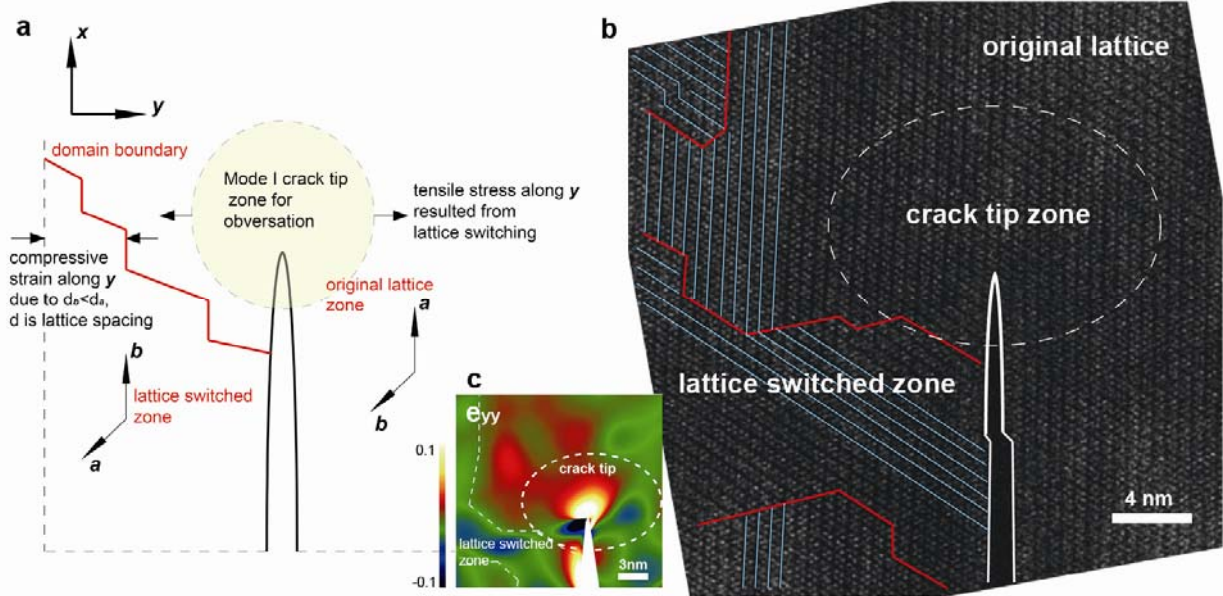
FIG. S6 Stress boundary conditions for the mode I crack tip zone. (a) Illustration of lattice switching which results the mode I loading in ReS$_2$. (b) Lower-magnification STEM image (lower than the *in situ* observation of crack propagation), showing the origin of mode I loading (lattice switching) corresponding to scheme in (a). (c) The GPA strain analysis result (normal strain, e$_{yy}$) corresponding to the STEM image in b. The crack tip zone (<5 nm, LEFM zone and nonlinear tip zone, discussed in main text) keeps the original lattice, while some other areas have been lattice-switched (*a* and *b*), and because the lattice spacings perpendicular to direction *a* (d$_a$) and perpendicular to direction *b* (d$_b$) are different, d$_a$ is the biggest lattice spacing for ReS$_2$, any lattice direction switch between *a* to *b* (or any type of switching other than *a* or *b*) will cause the compressive (contractive) strain in the lattice-switched zone, and then this lattice contraction due to d$_b$<d$_a$ outside of the crack tip zone will exert the tensile (pulling) load for the mode I crack, and cause opening stress (tensile stress) on crack tip zone. In all of the snapshots for fracture analysis, the region of crack tip zone is not lattice switched. The loading can be kept close to the Griffith loading (manifested by the strain analysis results (FIG. 4a and FIG. S12) and both the crack advance and heal can occur (FIG. 4a). At Griffith load, the lattice trapping barrier has the same height for crack advance and crack heal. If the loading is much higher than the current loading (Griffith load), the lattice trapping barrier will decrease significantly and the rate of crack advance will be much higher than the current level, and the intermediate states (unit cell by unit cell move) cannot be observed at the atomic scale by current (S)TEM method. Temporal resolution for our observation is between 10 ms~1 s, corresponding to a lattice trapping energy barrier height around 0.78 eV at room temperature. Due to electron beam, higher effective temperature can be applied for those crack moves when beam scanning over the crack tip, see FIG. 4). Therefore, our method which achieves to supply the Griffith load on the sample is prerequisite to observe the atomic scale propagation. Owning to the resolution requirement on image for strain analysis, in most of our *in situ* crack experiments, a higher magnification than image in *b* was applied, thus the lattice switching (domain reconstruction) cannot be recorded simultaneously with the crack tip zone, however the strain analysis (FIG. S10, S12) in crack tip

zone shows the typical mode I opening stress is always applied on the crack tip zone, and the origin can be attributed to the above lattice switching mechanism.
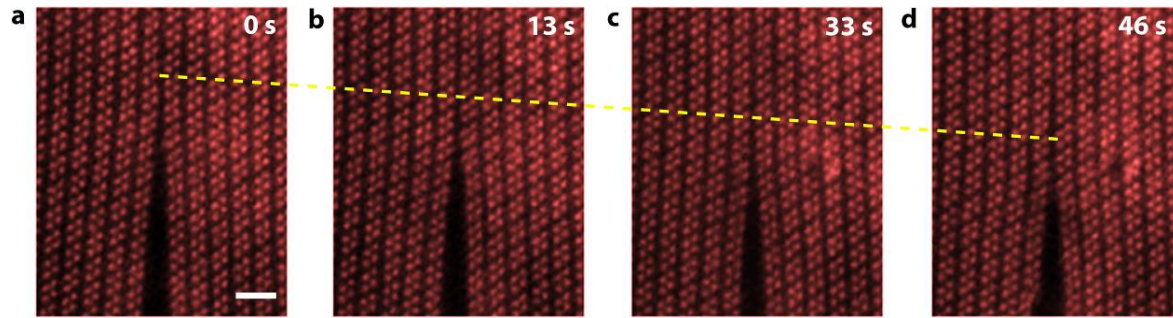

FIG. S7 Consecutive healing process of crack observed by *in situ* STEM. (a-d) The crack is consecutively healed at room temperature by three unit cells during 46 s. Yellow dashed line guides the eye for crack front positions. All images have been aligned to show the same position of specimen. Scale bar=1 nm.
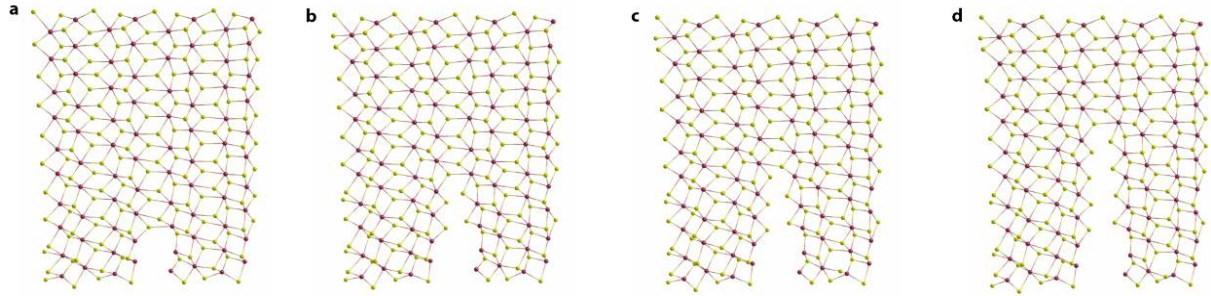
FIG. S8 DFT simulations on the Mode I crack of ReS$_2$. (a-d) The snapshots of continuous DFT simulations on the 10% strained ReS$_2$ structures with a pre-crack (removal of four S atoms) to manually introduce crack initialization. Purple atoms (Re), Yellow atoms (S).
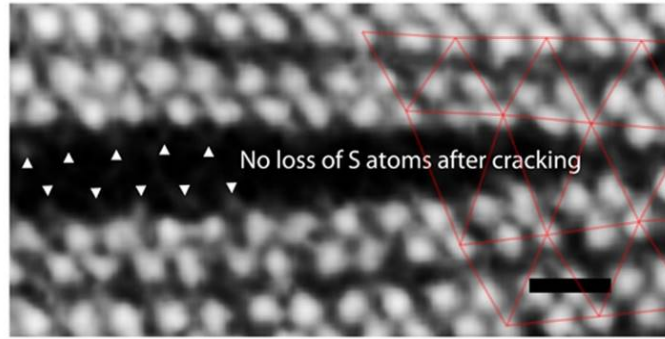
FIG. S9 HAADF image for one ReS$_2$ crack tip. White triangles highlight the S atoms on the edges. Red lattices show the discretized cells for strain analysis. Scale bar = 0.5 nm.
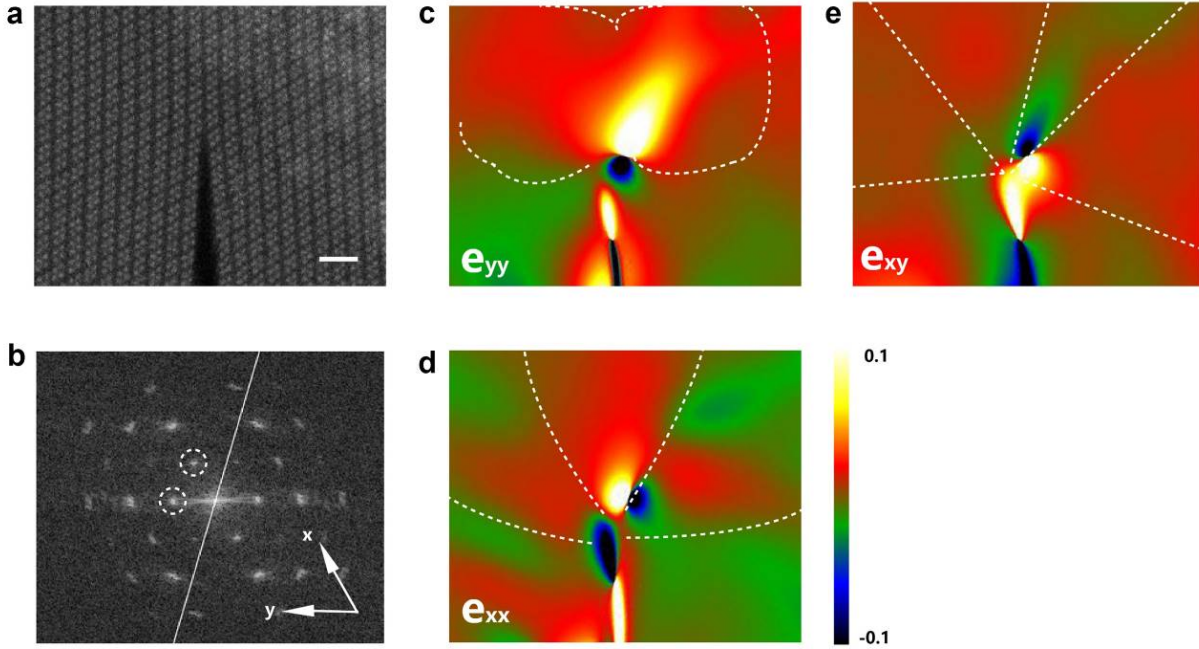
FIG. S10 The GPA analysis formalism and results to qualitatively present the strain distribution and comparison with the continuum fracture theory. The field distribution (normal strain and shear strain) in the fracture crack tips have similar distributions as the results of the asymptotic field in the continuum theories [31]. (a) The HAADF image of on-going mode I crack in monolayer ReS_2. (a),(c),(d),(e) have same scale, Scale bar=1 nm. (b) The Diffractogram showing the basic vectors defined for GPA. (c-e), The strain results (e_{yy}, e_{xx}, e_{xy}) corresponding to a, dashed contour lines guide the eyes for the comparison with the LEFM strain results for mode I cracks. The GPA results can be applied on the 1-5 nm region to the crack front, and the GPA results for the singular zones (such as the cracked vacuum zones and the <1 nm (nonlinear) region to the crack front) are not true.
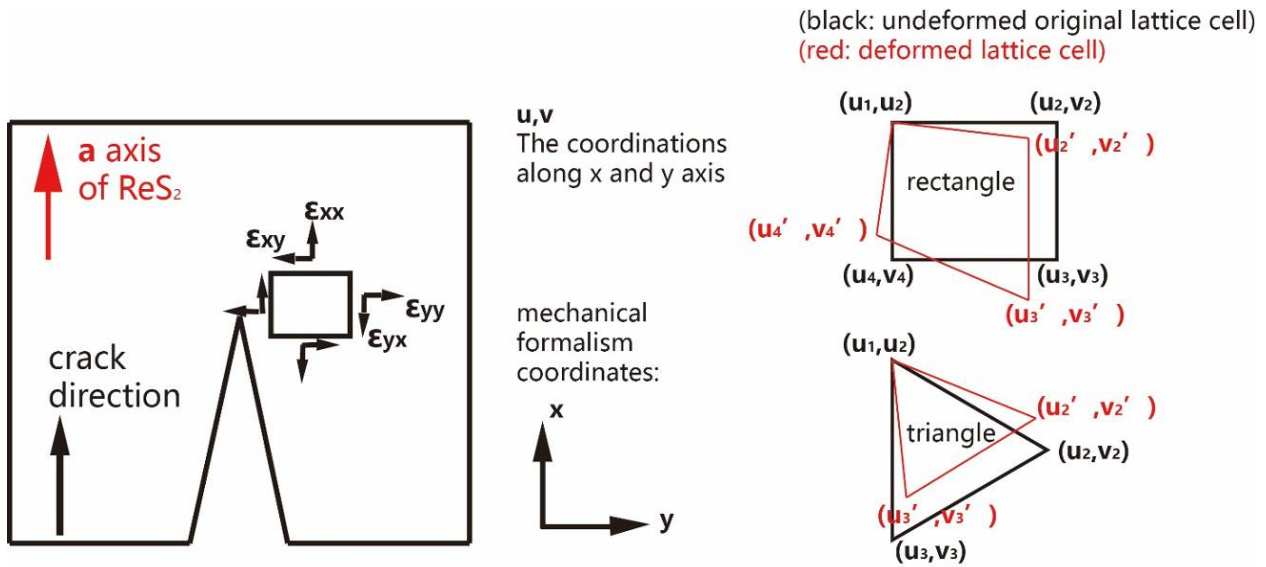
For each cell of atomic lattices,

1st step: calcualte strain of corner point pairs by using the undeformed states:

$$\{\varepsilon_{xx}, \varepsilon_{yy}, \varepsilon_{xy}\}=\{\partial u/\partial x, \partial v/\partial y, \partial u/\partial y+\partial v/\partial x\}$$

Then get the strain for each cell : linearly averaged

FIG. S11 The mechanical formalism for the discretized atomic scale strain, strain gradient and stress in this work. The strain and strain gradient are calculated by images(exp.)/lattice info(Sim.) as illustrated.
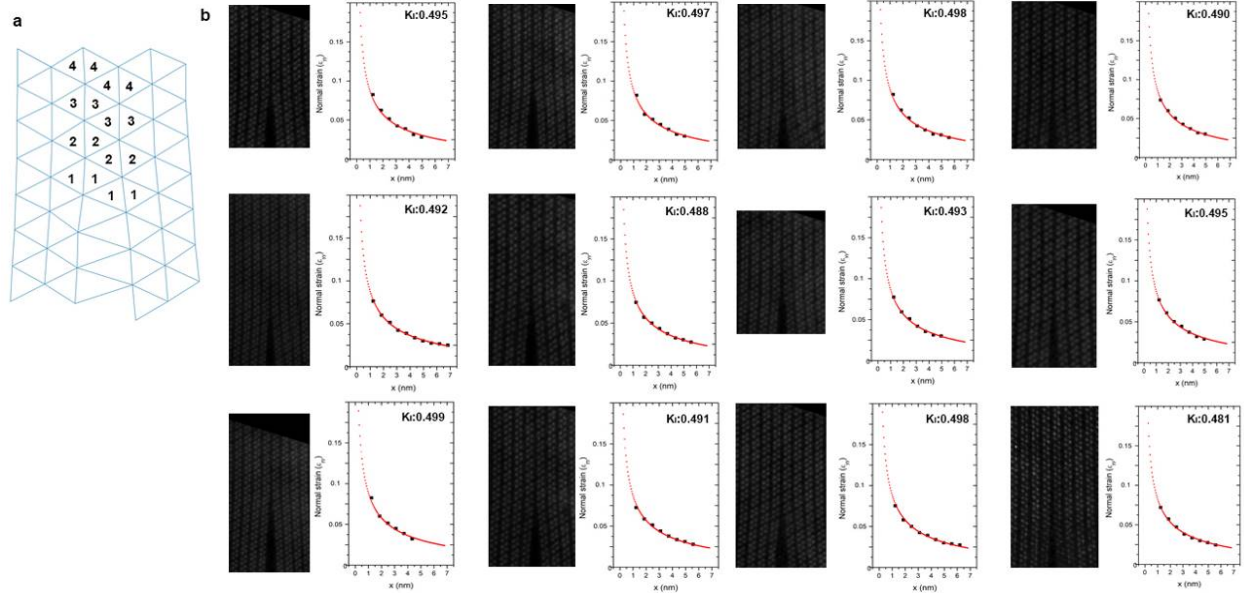
FIG. S12 Strain analysis and fitting with LEFM for the 1-5 nm region to the crack tip. (a) The scheme for the e_{yy} strain (tensile strain normal to crack direction) analysis compared with LEFM, the average strain values of four cells along the crack line are taken for each point (sampling position) in (b), number 1-4 marked each set of four cells for strain averaging, corresponding to the first four data points of each strain plot in (b). (b) Typical e_{yy} strain(black) along the crack line (x=distance to crack tip) for the mode I cracks in 1L ReS_2 with the LEFM fitting (red). The obtained K_I values of each snapshot are shown in the plot.
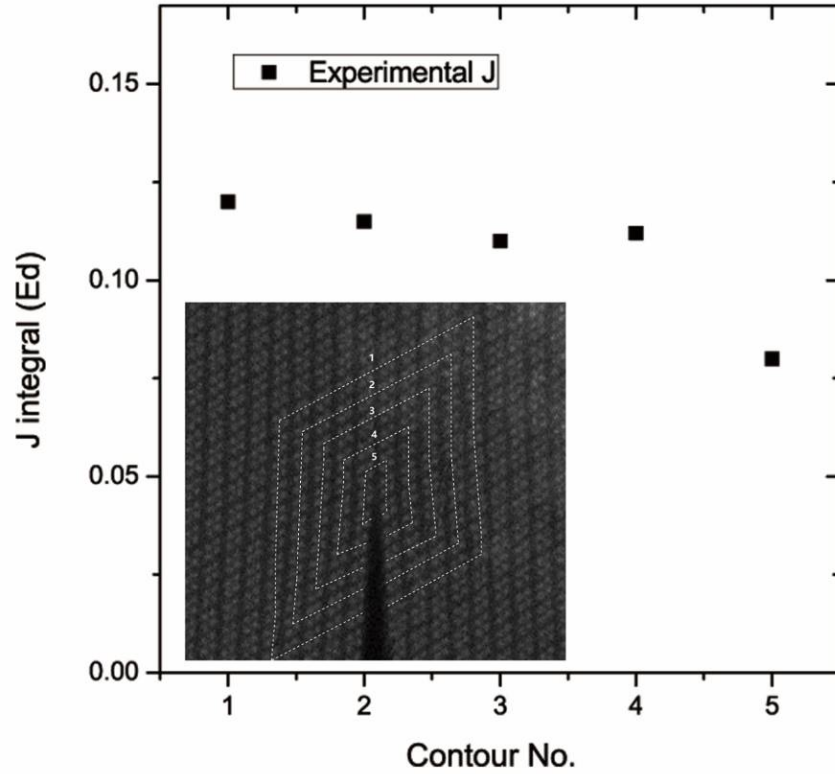
FIG. S13 The strain analysis on the crack tip zone with J integral methods. The two dimensional J integral calculated based on the atomic strain (J integral is path integrated along the dashed lines no. 1-5 shown in the inset, atomic strains are measured using same methods as described in methods of main text, and FIG. S12) for the five contours. Here J has the unit of Ed, where E is the young's modulus along y axis (shown in FIG. 2e), d is the lattice constant along x axis. The contours no. 1-4 have almost constant J values, in agreement with continuum theory, while for the contour no. 5 which locates inside the inner most region (around 1 nm zone within crack front), the J integral significantly deviated from no. 1~4 , exhibiting the nonlinear effect.
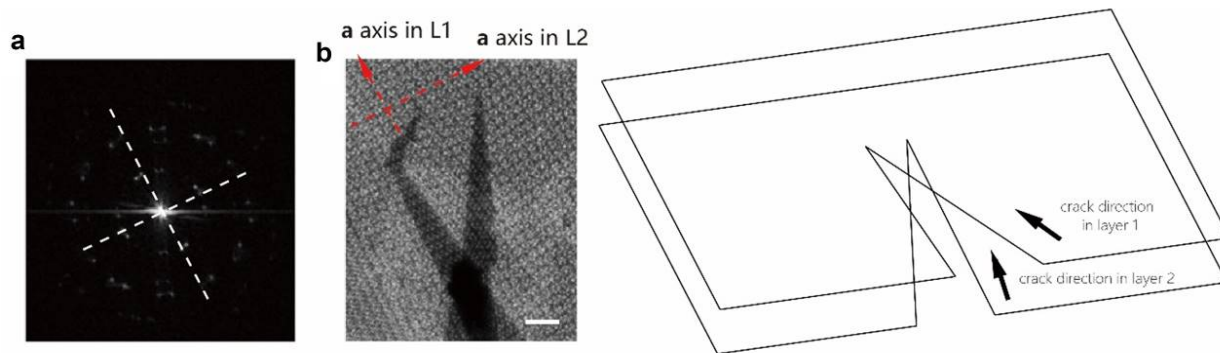
FIG. S14 Cracks in the incommensurately stacked bilayer ReS$_2$ which can roughen the crack edges. (a,b) The FFT and HAADF image for the crack tip zone, dashed lines mark the a axis directions in both layers. Scalebar = 1nm. (c) The scheme for the cracking in (b).
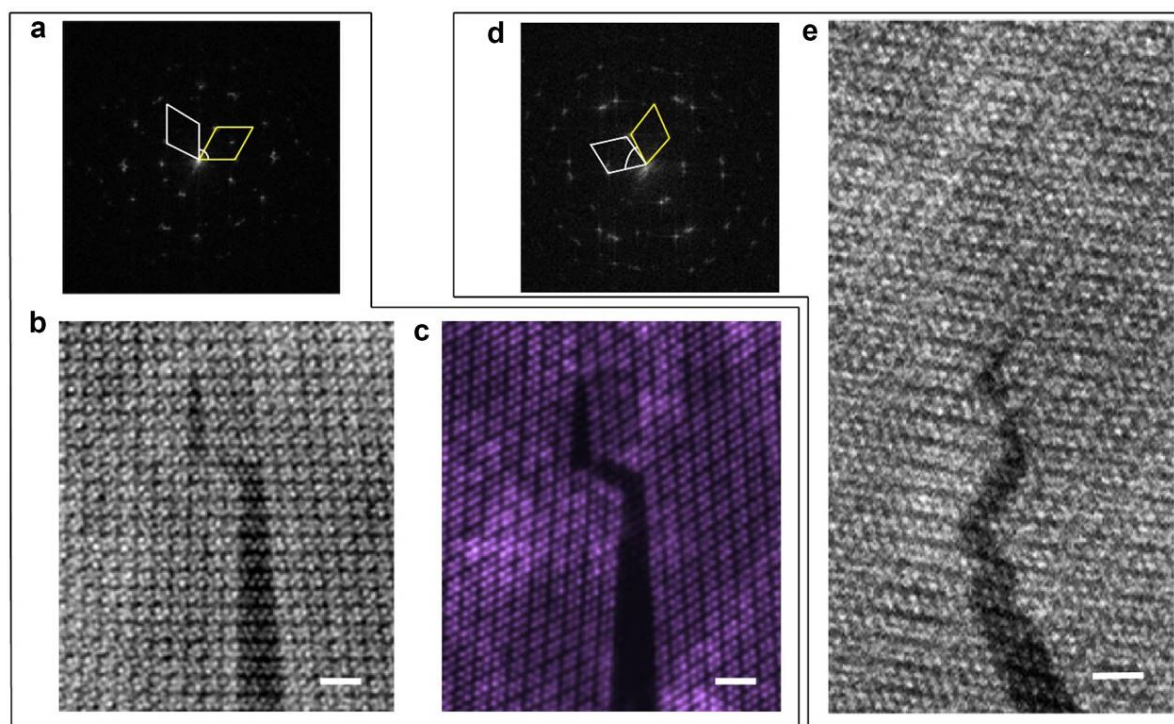

FIG. S15 Cracks in incommensurate bilayers. (a,b) The FFT and HAADF image of a leading crack in one layer and constrained by the other complete layer in incommensurate stacked bilayer ReS$_2$. (c) The cracked layer image reconstructed with the subset (yellow) of diffractogram shown in (a). (d,e) Another example of leading crack in one layer and controlled by the other layer in incommensurately stacked bilayer ReS$_2$. All scalebars = 1 nm.
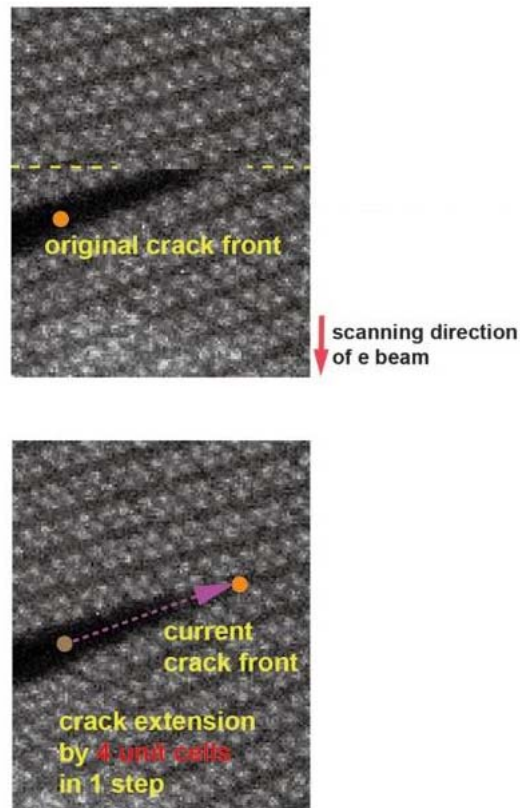
FIG. S16 The crack step measurement in crack event when the electron beam is scanning closely to the crack tip zone. Two consecutive STEM snapshots (~1s per image) of the same position in monolayer ReS_2 sample showing the crack instantly move by 4 unit cells when the beam scanning reaches the yellow dashed line position. The image below the yellow dashed line has identical crack opening, showing the crack does not move after the aforementioned one-time movement and before the lower part of image was taken. Hence the crack step (4 unit cells) for a "single" move within ~10 ms in this case can be determined. Electron beam size *ca.* 1.5Å. The e beam (thermal) activation effect can be included or excluded in our analysis (see main text related to FIG. 4b,c and FIG. S5b). In many other experimental cases, the crack tip keeps static during the beam scanning over the crack tip zone (no discontinuous line is found). The crack movement occurs during the beam scanning far away from the crack tip zone. Only by the consecutive two STEM images, the crack is found to move (move steps following $(1/4)^s$ decay), and in these cases the thermal energy activation (over lattice-trapping barrier) should be mainly responsible.
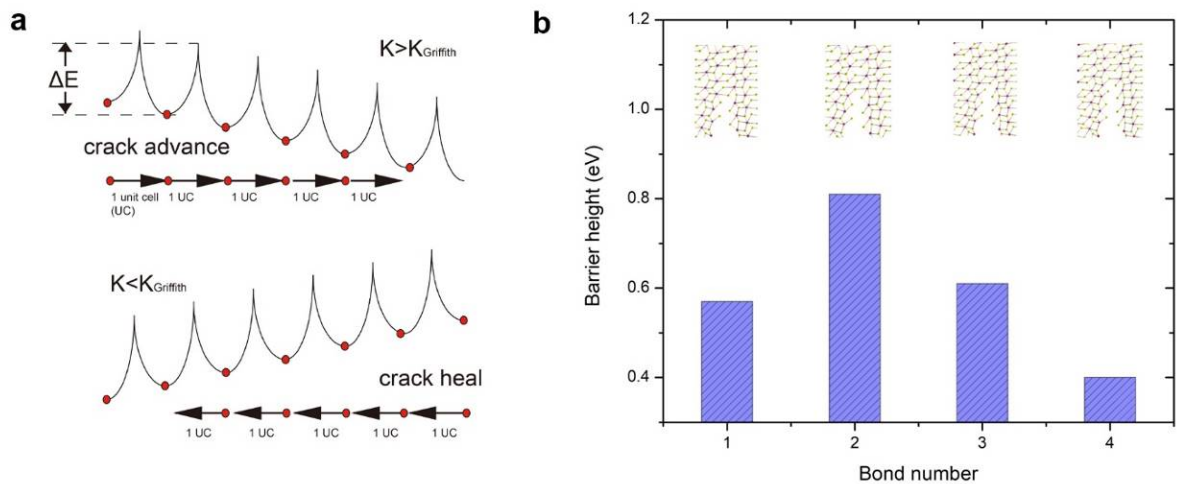
FIG. S17 (a) The scheme for the lattice trapping model and (b) DFT obtained energy barrier heights for four sub-barriers corresponding to four bonding ruptures.